Supplementary Information for "Interplay between gelation and glass formation in silica nanoparticle colloids"

Gianluca Gerardi, Christiane Alba-Simionesco, Manon Pépin, Anne Davaille

June 23, 2025

Supplementary Note 1: Coupling of DLVO and DMT models

We detail here how we couple the DLVO and DMT interactions in a unique, continue potential across the entire interparticle distance range. We start by recalling that a conservative force, by definition, is the first derivative of the potential, i.e. $F(x) = -\mathrm{d}V/\mathrm{d}x$ so that the DMT potential reads

$$V^{\mathrm{DMT}}(|\bar{h}_{ij}|) = C_2|\bar{h}_{ij}|^{5/2} - 2\pi R^* w|\bar{h}_{ij}|, \tag{1}$$

where $C_2 = (8/15)E^*R^{*1/2}$ and noticing that $\mathrm{d}|\bar{h}_{ij}|/\mathrm{d}\bar{h}_{ij} = -1$ for $\bar{h}_{ij} \leq 0$. Next, we ask for the continuity of the potential at $\bar{h}_{ij} = 0$, i.e. $V^{\mathrm{DMT}}(0) = V^{\mathrm{DLVO}}(0)$, which simply results in the addition of a constant in the DMT potential (which does not affect its derivative, thus, the force):

$$V^{\mathrm{DMT}}(|\bar{h}_{ij}|) = C_2|\bar{h}_{ij}|^{5/2} - 2\pi R^* w|\bar{h}_{ij}| + V^{\mathrm{DLVO}}(0). \tag{2}$$

Finally, we impose the continuity of the force at contact, i.e. $F_{ij}^{\mathrm{DMT}}(0) = F_{ij}^{\mathrm{DLVO}}(0)$, which results in the following expression for the adhesion energy:

$$\begin{aligned} w = \frac{A_{\mathrm{H}}}{12\pi h_0^2}\left[\frac{8R(2R+h_0)}{(4R+h_0)^2} + \frac{8Rh_0^2}{(2R+h_0)^3} - \frac{16Rh_0^2}{(4R+h_0)(2R+h_0)}\right] - \\ - \frac{A_Y}{\pi R\left(1+\mathrm{e}^{\kappa h_0}\right)}. \end{aligned} \tag{3}$$

Note that the above exact expression reduces to

$$w \approx \frac{A_{\mathrm{H}}}{12\pi h_0^2} - \frac{A_Y}{2\pi R}, \tag{4}$$

observing that $R \gg h_0$ and $\mathrm{e}^{\kappa h_0} \approx 1$. Furthermore, for the range of parameters adopted in the study, the negative term related to the electrostatic repulsion in (4) varies between $0.3 - 0.5$ mJ/m^2 which is small compared to the value of ≈ 7 mJ/m^2 determined by the first term in (4).

Below, we summarize the expressions implemented in LAMMPS which result from the coupling of DLVO and DMT interactions:

$$V(\bar{h}_{ij}) = \begin{cases} -\dfrac{A_H}{6}\left(\dfrac{2R^2}{(\bar{h}_{ij}+h_0)^2+4(\bar{h}_{ij}+h_0)R} + \dfrac{2R^2}{\left(\bar{h}_{ij}+h_0+2R\right)^2} + \right. \\ \left. +\ln\left[1-\left(\dfrac{2R}{\bar{h}_{ij}+h_0+2R}\right)^2\right]\right) + \dfrac{A_Y}{\kappa}\ln\left(1+\mathrm{e}^{-\kappa\left(\bar{h}_{ij}+h_0\right)}\right) & \text{for } 0 \leq \bar{h}_{ij} \leq h_c\,, \\ \\ C_2|\bar{h}_{ij}|^{5/2} - 2\pi R^* w|\bar{h}_{ij}| + V^{\mathrm{DLVO}}(0) & \text{for } \bar{h}_{ij} \leq 0, \end{cases} \tag{5}$$

$$F_{ij}(\bar{h}_{ij}) = \begin{cases} -\dfrac{A_H}{6}\left[\dfrac{4R^2\left(\bar{h}_{ij}+h_0+2R\right)}{\left(\bar{h}_{ij}+h_0\right)^2\left(\bar{h}_{ij}+h_0+4R\right)^2}+\dfrac{4R^2}{\left(\bar{h}_{ij}+h_0+2R\right)^3}-\right. & \\ \left.-\dfrac{8R^2}{\left(\bar{h}_{ij}+h_0\right)\left(\bar{h}_{ij}+h_0+2R\right)\left(\bar{h}_{ij}+h_0+4R\right)}\right]+ & \\ +\dfrac{A_Y}{1+\mathrm{e}^{\kappa\left(\bar{h}_{ij}+h_0\right)}} & \text{for } 0 \le \bar{h}_{ij} \le h_c, \\ \dfrac{5}{2}C_2|\bar{h}|^{3/2} - 2\pi R^* w & \text{for } \bar{h}_{ij} < 0. \end{cases} \tag{6}$$

h_c is the long range cutoff of the potential, set to the particle radius in the study, and w is computed through (3).

Supplementary Note 2: Equilibration runs and long-term diffusion coefficient

In Supplementary Fig. 1 we show the time evolution of the average contact number $< z >$, i.e. the average number of contacts per particle, for different values of ϕ. We consider the system at the equilibrium when $< z >$ reaches a steady-state value. For the majority of configurations, this occurs at $t \approx 10^2 \tau_S$. However, for the dilute cases ($\phi \le 0.28$), the system reaches a steady state much earlier, at $t \approx \tau_S$.

Supplementary Fig. 2 illustrates the time evolution of the Mean Squared Displacement (MSD), normalized by the particle diameter $2R$, for the same configurations shown in Supplementary Fig. 1. The slope of the MSD curve (inset of Supplementary Fig. 2) represents the diffusion coefficient, which reads

$$\mathcal{D} = \frac{1}{6}\frac{\mathrm{d}\,(\mathrm{MSD})}{\mathrm{d}t}. \tag{7}$$

The diffusion coefficient is normalized by the classical Stokes-Einstein coefficient $\mathcal{D}_0 = k_B T/(6\pi\eta_s R)$. The equilibrium values of $\mathcal{D}/\mathcal{D}_0$ reported in the main text of the paper are obtained from the mean of $\mathcal{D}/\mathcal{D}_0(t/\tau_S)$ for $t/\tau_S \gg 1$, where $\mathcal{D}/\mathcal{D}_0$ remains approximately constant (see dashed lines of the inset of Supplementary Fig. 2).

In Supplementary Fig. 3 we show the effect of the initial conditions on the evolution of $< z >$ (Supplementary Fig. 3 **(a)**) and of the normalized MSD (Supplementary Fig. 3 **(b)**). For each value of ϕ considered, the ensemble average (solid line) is obtained from four different configurations with different initial conditions (dashed black lines). Both the equilibrium structural information ($< z > (t/\tau_S \gg 1)$) and the dynamical information (MSD$(t/\tau_S \gg 1)$) show a very weak dependence on the initial conditions. Indeed, both quantities vary by less than 1% across the different runs.

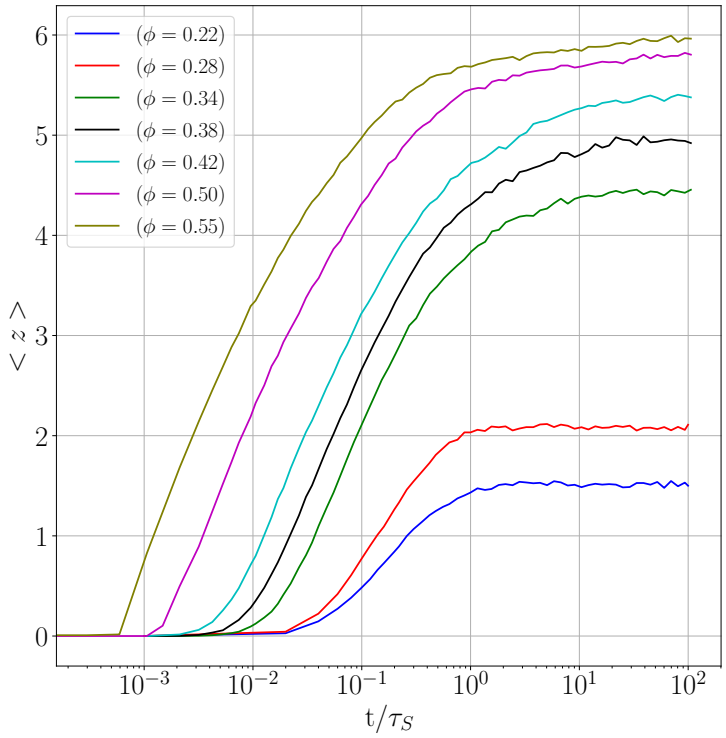

Supplementary Fig. 1: Time evolution of the average contact number $< z >$. Each curve represents a system characterized by a different particle volume fraction ϕ, as indicated in the legend.

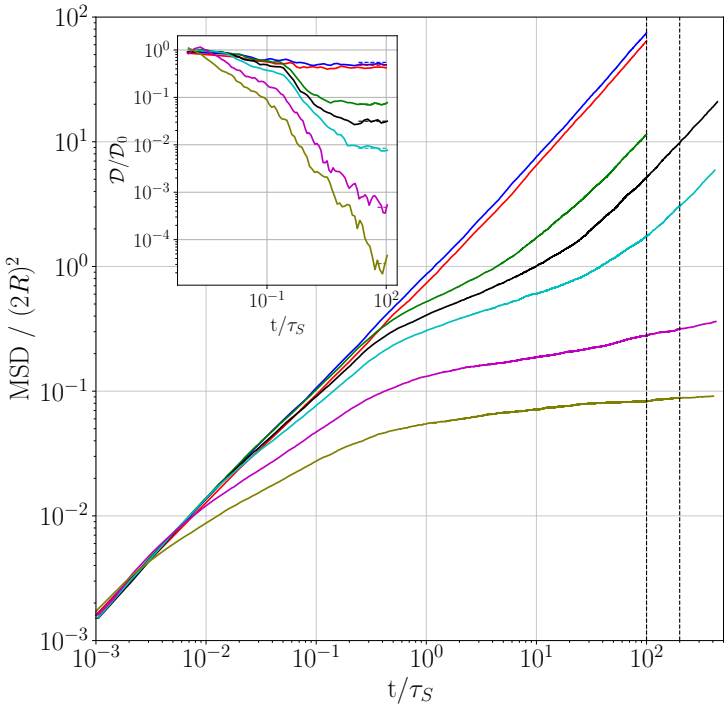

Supplementary Fig. 2: Time evolution of the normalized Mean Squared Displacement (MSD) for $0.22 < \phi < 0.55$. The color code identifying the configurations with different ϕ is the same as shown in Supplementary Fig. 1. The evolution of the relative diffusion coefficient $\mathcal{D}/\mathcal{D}_0$ is shown in the figure inset. Here, the colored dashed lines represent the mean value of $\mathcal{D}/\mathcal{D}_0$ taken for $t/\tau_S \gg 1$, which is representative of the equilibrium state. Simulations are extended for dense configurations ($0.38 \leq \phi \leq 0.55$). The two vertical dashed lines indicate the time window $100 \leq t/\tau_S \leq 200$, corresponding to the trajectories used for the multi particle tracking analysis discussed in Supplementary Note 5.

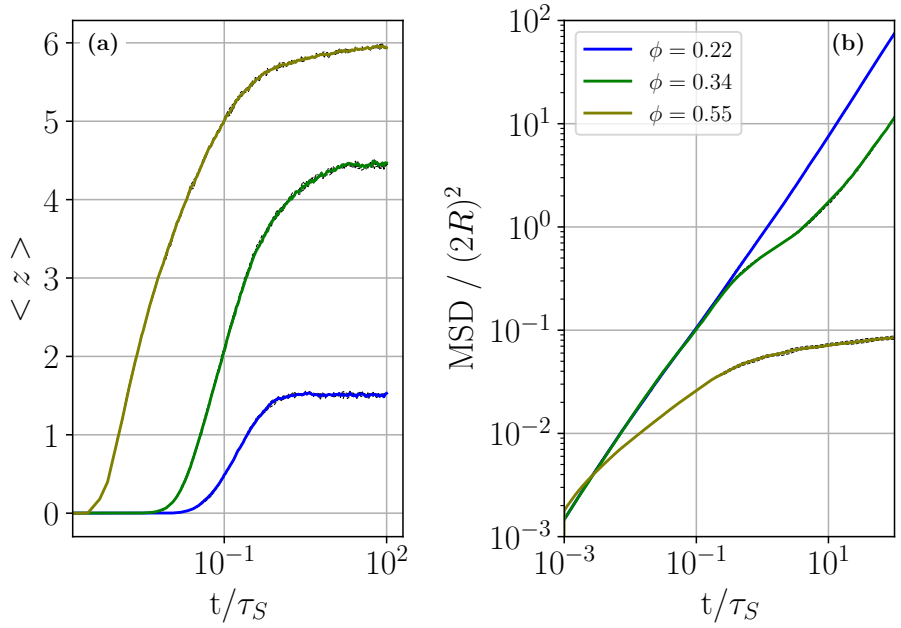

Supplementary Fig. 3: Ensemble averages (solid colored lines) obtained from four different runs (black dashed lines) of the time evolution of: **(a)** $< z >$; **(b)** normalized MSD. The legend in **(b)** reports the values of ϕ characterizing the different systems. Note that, especially in **(b)**, the variation across the different configurations (for a fixed value of ϕ) is so small that it is almost completely hidden by the width of the solid line.

Supplementary Note 3: DSC experimental measures

Supplementary Fig. 4 shows the results of the DSC measurements done on different samples of LudoxHS40, characterized by a particle volume fraction $0.378 < \phi < 0.403$. For water nanocrystals melting in a solid structure composed of silica nanoparticles, the characteristic size of the nano-sized pores can be evaluated with the fitting equation proposed by [1], i.e.

$$< C_{\mathrm{S}} >= 95/\Delta T_m, \tag{8}$$

where $\Delta T_m = T_{m,bulk} - T_{m,pore}$, is the difference between the melting temperatures of the bulk (*free*) water crystals ($T_{m,bulk}$) and of the confined water nanocrystals ($T_{m,pore}$). When typical values of $< C_{\mathrm{S}} >$ are lower than 6 nm the effect of a thin layer of water which has not crystallized needs to be taken into account [2]. In this case eq. (8) modifies as

$$< C_{\mathrm{S}} > /2 = 49/\Delta T_m + 0.6, \tag{9}$$

where we consider a typical value of 0.6 nm for the non-crystallized thin water film.

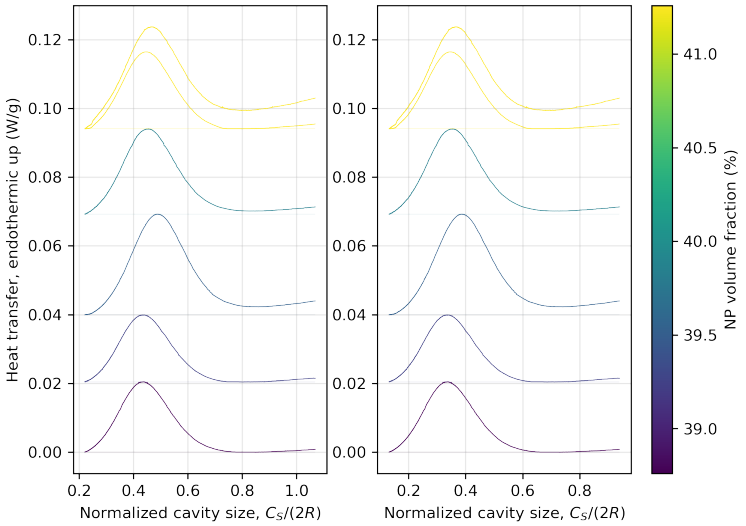

Supplementary Fig. 4: DSC thermograms of LudoxHS40 samples characterized by $0.378 < \phi < 0.403$. The heat flow on the vertical axis is reported as a function of the cavity size on the horizontal axis. The latter is obtained from the temperature recorded during the experiments, using equation (8) (right figure) or equation (9) (left figure). The peak in heat flow marks the phase transition of water, thereby identifying the characteristic size of the cavities trapping the water crystals. Data from [2].

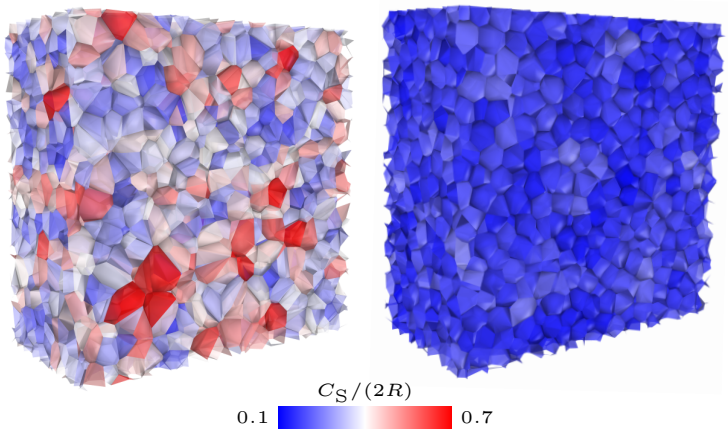

Supplementary Fig. 5: A 3D cut of the Voronoi tessellation describing the spatial distribution of cavity sizes for two systems: $\phi = 0.34$ (left), $\phi = 0.55$ (right). The color of the Voronoi cells reflects the value of the (normalized) cavity size, as estimated with eq. (1) reported in the main text.

Supplementary Note 4: Cavity size distribution

To illustrate the evolution of the spatial distribution of cavity sizes with increasing particle volume fraction, we report in Supplementary Fig. 5 the cavity sizes derived from the Voronoi tessellation of two representative configurations ($\phi = 0.34$ and $\phi = 0.55$), corresponding to the end-members discussed in § 2.2 of the main text. We can appreciate how the less concentrated configuration ($\phi = 0.34$, left panel) exhibits a heterogeneous distribution of cavity sizes, whereas the system at $\phi = 0.55$ (right panel) displays a pronounced spatial homogenization of cavity sizes. Corresponding 3D renderings of these two configurations are provided in movies "Phi_034.avi" and "Phi_055.avi".

Supplementary Note 5: Multi particle tracking analysis

To characterize the single particle mobility for the dense configurations, i.e. $0.38 \leq \phi \leq 0.55$, we record the particle trajectories in the time interval $100 \leq t/\tau_S \leq 200$ (see Supplementary Fig. 2). The MSD of a single particle is time-averaged for a given lag time τ as described in [3]:

$$\mathrm{MSD}\,(\tau = n\Delta t) = \frac{1}{N-n}\sum_{j=1}^{N-n}\left|\mathbf{r}(j\Delta t + \tau) - \mathbf{r}(j\Delta t)\right|^2, \tag{10}$$

where N is the number of points recorded in the $100\,t/\tau_S$ long trajectory. In our analysis, we use $N = 2000$, which provides a good statistical sample for the time-averaged MSD up to $\tau/\tau_S = 1$. The MSD (τ) curves obtained with eq. (10) are shown in Supplementary Fig. 6.

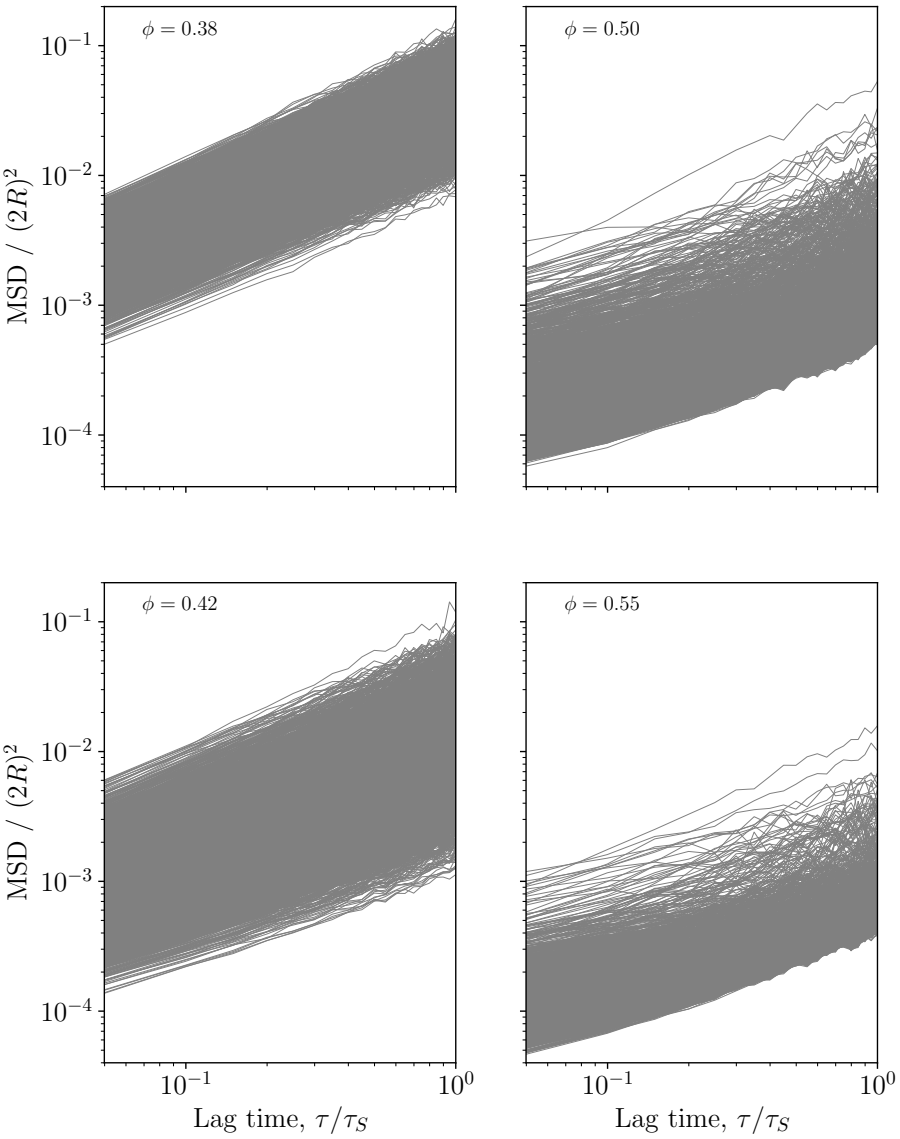

Supplementary Fig. 6: Normalized single-particle (time-averaged) MSD as a function of the normalized lag time for the four dense configurations $\phi = 0.38$, $\phi = 0.42$, $\phi = 0.50$ and $\phi = 0.55$.

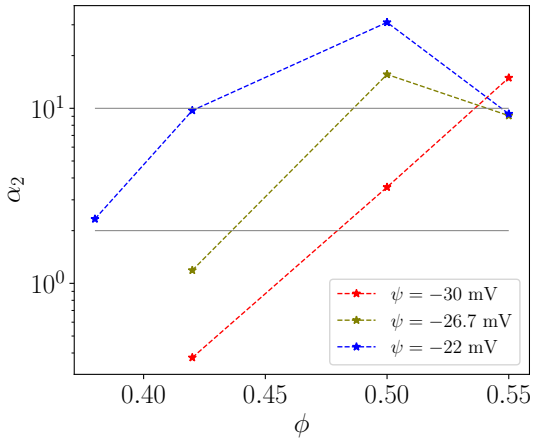

Supplementary Fig. 7: α_2 as a function of ϕ, for three different values of ψ. The dashes lines are to guide the eye. The two horizontal gray lines highlight the values $\alpha_2 = 2$ and $\alpha_2 = 10$. The points characterized by $\alpha_2 \approx 2$ ($\phi = 0.38, \psi = -22$ mV) and $\alpha_2 \approx 3.5$ ($\phi = 0.50, \psi = -30$ mV) correspond to the two points in Fig. 9**(b)** of the main text, enclosed in the small gray circle. The points characterized by $\alpha_2 \geq 10$ correspond to the five points in Fig. 9**(b)**, enclosed in the bigger gray circle.

Supplementary Note 6: Effect of electrostatic repulsion on the non-Gaussian parameter

We report in Supplementary Fig. 7 the evolution of the non-Gaussian parameter α_2 for dense configurations ($\phi \geq 0.38$) and different electrostatic strengths (i.e. different values of ψ). In general, for a fixed value of ϕ, α_2 tends to be lower at higher values of ψ, indicating that stronger electrostatic repulsion delays the onset of glassy dynamics in this colloidal system.

Moreover, the peak of α_2, associated wit the emergence of an arrested amorphous solid state, appears to shift toward higher particle volume fractions as electrostatic repulsion increases. This trend is particularly evident for the strongest repulsion condition (red data points, $\psi = -30$ mV), where α_2 exhibits a monotonic increase with ϕ, reaching its maximum for $\phi \geq 0.55$.

References

1. Lu, Y., Liu, Y., Xu, Y., Wang, L. & Li, J. Size-dependent melting of ice in mesoporous silica. *Philosophical Magazine* **93,** 1827–1842 (2013).
2. Pépin, M. *Relation structure-rhéologie dans les suspensions nanocolloïdales* PhD thesis (Université Paris-Saclay, Orsay, 2025).
3. Schirripa Spagnolo, C. & Luin, S. Trajectory Analysis in Single-Particle Tracking: From Mean Squared Displacement to Machine Learning Approaches. *International Journal of Molecular Sciences* **25,** 8660 (2024).